

# Performance Optimizations and Evaluations for the Small Direct Currents Measurement System

---

Shunyi Liang<sup>a</sup> Juncheng Liang<sup>b,1</sup> Kezhu Song<sup>a,1</sup> Yijie Jiang<sup>a</sup> and Zhijie Yang<sup>b</sup>

<sup>a</sup>State Key Laboratory of Particle Detection and Electronics,  
University of Science and Technology of China,  
Hefei 230026, China

<sup>b</sup>National Institute of Metrology,  
Beijing 100029, China

E-mail: [liangjc@nim.ac.cn](mailto:liangjc@nim.ac.cn), [skz@ustc.edu.cn](mailto:skz@ustc.edu.cn)

**ABSTRACT:** Ionization chambers are essential for activity determinations in radionuclide metrology. We have developed a high-precision integrating-differentiating (int-diff) system for measuring small currents. It is anticipated to enhance the ionization current measurement capability of the  $4\pi\gamma$  ionization chamber radioactivity standard at the National Institute of Metrology (NIM), China. Besides, it has broad application prospects in physical experiments and fundamental metrology. The design of the measurement system is optimized through circuit analysis and simulation. The structure of the integrating capacitor array is redesigned to reduce the error of the amplification gain, and a relay is used as the reset switch to achieve improved noise and bias. The digital readout and control module is also enhanced in terms of flexibility and functionality. High-precision test platforms utilizing the standard small current source at NIM China and an ionization chamber were developed to evaluate the performance of the system. The results demonstrate an ultra-low noise floor ( $<1$  fA/ $\sqrt{\text{Hz}}$ ) and a low current bias ( $<1$  fA), as well as a low temperature coefficient of the amplification gain of 2.1 ppm/ $^{\circ}\text{C}$ . The short-term stability and linearity of the gain are also tested and exhibit comparable indicators to those of the Keithley 6430. Reasonable results are obtained in the long-term reproducibility test. Therefore, the system enables high-precision measurements for small direct currents and shows promise for applications in ionization chambers.

**KEYWORDS:** Analysis and statistical methods, Data acquisition circuits, Data processing methods, Digital signal processing (DSP), Dosimetry concepts and apparatus, Front-end electronics for detector readout, Gaseous Detectors, Instrument optimisation

---

<sup>1</sup>Co-corresponding authors.

---

## Contents

|          |   |           |
|----------|---|-----------|
| <b>1</b> | <b>Introduction</b>   | <b>1</b>  |
| <b>2</b> | <b>Measurement System Architecture</b>                      | <b>2</b>  |
| 2.1      | Front-End Circuit Design                                    | 2         |
| 2.2      | Read-out and Control Design                                 | 5         |
| <b>3</b> | <b>Performance Test Platforms and Results</b>               | <b>6</b>  |
| 3.1      | Current Bias and Noise Tests                                | 6         |
| 3.2      | Stability Tests   | 8         |
| 3.3      | Long-term Reproducibility Test Utilizing Ionization Chamber | 12        |
| <b>4</b> | <b>Conclusions</b>  | <b>14</b> |

---

## 1 Introduction

Accurate measurement of small currents ranging from femtoamperes to nanoamperes is essential in radionuclide metrology. In the process of activity determinations, a factor that often restricts the uncertainty lies in the measurement of the ionization current[1]. In recent years, picoampere-meters (picoammeters) have attained higher levels of precision and have been widely applied in various fields, including fundamental metrology [2], physical experiments [3], and biosensors[4]. In the National Institute of Metrology (NIM), China, researchers are dedicated to improving the  $4\pi\gamma$  ionization chamber (IC) radioactivity standard, thereby raising the demand for high-precision picoammeters.

The ultra-stable low-noise current amplifier (ULCA), based on the feedback trans-impedance amplifier (TIA) structure, was introduced by the Physikalisch-Technische Bundesanstalt (PTB). Its key element, the resistor array, provides very stable amplification gain, enabling achievement of the state-of-the-art uncertainty of 0.1 ppm in 100 pA [5]. The well-known commercial electrometers Keithley model 6430 and Keysight model B2980 both employed TIA to amplify small currents, and they have multiple ranges and functionalities to support different scenarios [6, 7]. The TIA structure is relatively mature and precise, and it's widely applied in recent researches [8–10]. However, limited by the precision resistor techniques, large resistors providing high gain are basically less precise and less stable. In comparison with another structure known as the shunt amplifier, the TIA structure can be more precise for its low input burden voltage, but the shunt type is more commonly seen in portable multi-meters because its simpler circuit and lower cost [3, 11]. Certain studies adopted the integrating-differentiating (int-diff) structure to achieve the least noise level by replacing the TIA's noisy feedback resistor with a capacitor in the integrating stage (integrator) [4, 12]. Other than ultra-low noise performance, this structure can also accomplish high bandwidth that more than 100 kHz [13]. However, its drawbacks are as follows: the capacitor significantly influences

the precision and stability of the gain as well as the analog differentiating stage can introduce nonlinearity errors. Thus previous researches on this kind of amplifiers seldom took into account the stability and precision for DC measurements [4].

In our previous work [14], we proposed a precise small currents measurement system (SCMS). This system is based on the int-diff method to achieve low noise. It integrates the direct current (dc) in the analog amplification circuit and differentiates it in a field programmable gate array (FPGA) to restore a dc output. The analog circuit combines careful circuit design and techniques. For instance, by means of the averaging effect of the integrating capacitor array, we took stability into considerations.

In this paper, we further optimized the design of the SCMS through analysis and simulation, and conducted more comprehensive tests. The capacitor array structure was optimized through simulations to suppress gain errors due to parasitic capacitance. We substituted the CMOS-based switches with a reed relay, and noted improved noise and current bias performance. Additionally, the host software of the SCMS is upgraded to enhance its functionality. We also developed different test platforms utilizing the standard small current source equipment at NIM China and a  $4\pi\gamma$  IC to evaluate various performance indicators of the SCMS. The test results exhibits ultra low noise floor ( $<1\text{ fA}/\sqrt{\text{Hz}}$ ) and current bias ( $<1\text{ fA}$ ), low temperature coefficient ( $2.1\text{ ppm}/^\circ\text{C}$ ), short-term stability and linearity similar to that of the Keithley 6430, as well as reasonable long-term reproducibility for an IC application.

The paper is organized as follows: In Section 2, the architecture of the SCMS is introduced, with a primary focus on the optimizations made to its design. Section 3 presents the test setups devised for evaluating noise and stability performances and provides an analysis of the test results. Section 4 concludes the paper.

## 2 Measurement System Architecture

In our previous work [14], we put forward a precise small currents measurement system. It has a basic structure as shown in fig. 1, including the analog front-end circuit and the digital readout and control module. The system is extensible to support the simultaneous reading of two front-end circuits, thereby improving the signal-to-noise ratio by measuring the current twice. The measurement system is designed with a integrating-differentiating (int-diff) scheme, One of our innovations is the analog-integrating and digital-differentiating method. Since we don't use an analog differentiating circuit, such as a conventional correlated double sampling (CDS) circuit that can be an error source for the sample and hold circuit [15, 16], our structure ensures high precision and flexibility in the data processing.

### 2.1 Front-End Circuit Design

The most critical part of this design is the front-end amplification circuit. It comprises two stages, namely the low-noise integrating stage (integrator circuit), and the voltage amplification stage. Figure 2 illustrates the basic structure of the two-stage amplification circuit. The first stage integrates current to voltage ramp through a capacitor, and the second stage provides 10-fold inverting voltage gain. The slope of the output signal is related to the measured input current with

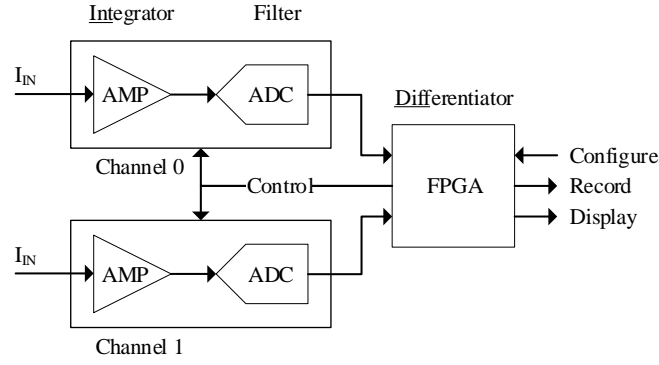


**Figure 1.** Overall architecture of the SCMS.

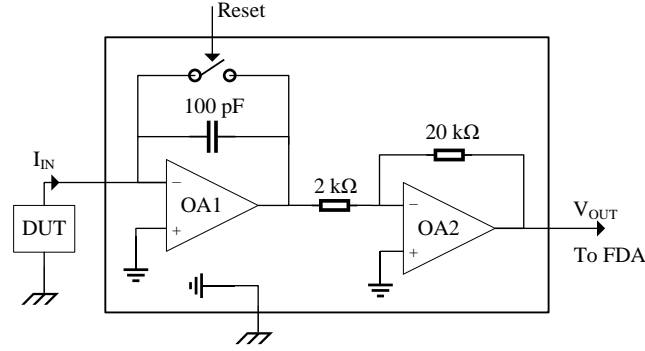


**Figure 2.** Simplified schematic of the analog amplification circuit.

an equivalent trans-resistance gain  $G_{TR}$  of

$$G_{TR} = \left(-\frac{T_i}{C_i}\right) \times \left(-\frac{R_f}{R_i}\right), \quad (2.1)$$

where  $T_i$  and  $C_i$  are the integrating time and 100 pF integrating capacitor, and  $R_f$  of 20 k $\Omega$  along with  $R_i$  of 2 k $\Omega$  are the feedback and input resistors of the second stage. The integrator needs to be periodically reset by a switch to ensure that the output voltage will not saturate.

To minimize the insulation resistances (IR) and improve the precision and stability, 100 capacitors are arranged in serial and parallel configuration to form the equivalent 100 pF integrating capacitor. The IR can be simply regarded as being connected in parallel with the integrating capacitor, thereby forming an RC circuit and resulting in an integrating error relative to the first stage gain[14],

$$\delta_{int} = n(1 - e^{-1/n}) - 1, \quad (2.2)$$

where  $n = R_{IR}C_i/T_i$ , and  $R_{IR}$  represents the total IR. Each capacitor is a class I ceramic capacitor (provided by KEMET) with more than 100 G $\Omega$  IR, low tolerance and low temperature coefficient. We improved the structure of the integrating capacitor array in comparison to the previous 100

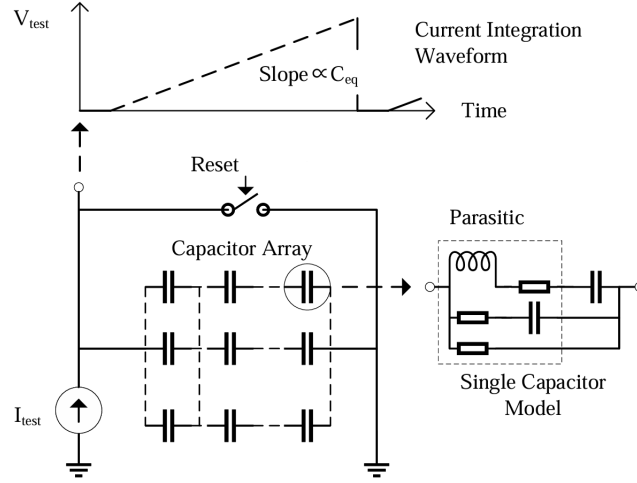


**Figure 3.** Illustration of the parasitic capacitance modeling circuit, assuming an ideal reset switch and an ideal testing current source, with multiple configurations for connecting the capacitor array. The equivalent capacitance is assessed by analyzing the slope of the current integration waveform.

serial-connected capacitor array. To account for the more intricate parasitics of the capacitors, we constructed dedicated simplified circuit models simulating and analyzing the capacitor array performance, as illustrated in fig. 3.

The simulations involved three main steps: netlist editing, circuit solving, and data analysis. Circuit solving was conducted using a simulation program with integrated circuit emphasis, while Python was employed to enhance the other steps, especially for simulating complex circuits [17]. The capacitor array was evaluated from the tolerance of the equivalent capacitance ( $C_{eq}$ ) and the nonlinearity error of the current integrating waveform. Firstly, tolerance is calculated as the relative deviation between the measured and nominal values of  $C_{eq}$ . We conducted Monte Carlo simulations, where the capacitor's value follows a normal distribution. Secondly, the nonlinearity error  $\delta_{int}$  is determined as the maximum relative residual of the linear fit to the integration waveform.

Simulations revealed that tolerance and nonlinearity error are influenced by the array structure and capacitor selection, necessitating comprehensive considerations. Table 1 presents the performance of various capacitor arrays, each identified by an abbreviated label indicating its structure. For instance, 'pX-sY' denotes X capacitors in parallel, forming a block, with Y blocks connected in series. The results demonstrate that the 's5-p5-s4' structure, utilizing 430 pF 0603 capacitors, achieves optimal performance.

A parasitic capacitance at the pF level paralleled to the integrating capacitor is observed, which directly affects the equivalent capacitor precision. The PCB parasitic capacitance was evaluated and optimized through post-layout simulation using Cadence PowerSI. It is calculated in (2.3) based on the simulated impedance ( $Z_C$ ) at low frequencies.

$$C_p = \frac{1}{2\pi f Z_C}. \quad (2.3)$$

We optimized the PCB layout by arranging the capacitor array tightly, removing the connector and raising the height between the signal and reference layers. Simulation result indicates that the

**Table 1.** Simulated Performance Comparison of Various Capacitor Array Configurations.

| structure  | capacitor   | $C_{eq}$ | tolerance | nonlinearity |
|------------|-------------|----------|-----------|--------------|
| s10-p10-s4 | 430 pF 0805 | 107.5 pF | 0.068 %   | 39.4 ppm     |
| s5-p5-s4   | 430 pF 0603 | 107.5 pF | 0.022 %   | 6.8 ppm      |
| s100       | 10 nF 0603  | 100 pF   | -0.53 %   | 31.6 ppm     |
| s20-p20    | 100 pF 0603 | 100 pF   | 0.702 %   | 180 ppm      |
| s10-p10-s4 | 430 pF 0603 | 107.5 pF | 0.039 %   | 7.42 ppm     |

parallel parasitic capacitance decreases from 8 pF to 3 pF.

The reset switch is enhanced by substituting the CMOS-based switch with the signal relay. Although the CMOS-based switch offers high switching speed, the signal relay (provided by Panasonic) exhibits ultra-low leakage current and inherent noise characteristics, as verified in section 3. The drawbacks of the relay switch include a lower switching speed and significant signal fluctuations within approximately 100 ms after the switch is opened (current integrating phase). The fluctuation may be caused by the fact that this relay is not shielded, and the switch control signal is coupled into the current trace. We solved this issue by employing long integrating-reset period of 0.5 s, and discarding the first 100 ms data after the switch is opened.

The ADA4530 with fA-level bias current is selected as the first-stage operational amplifier, whereas the second-stage uses the ADA4625 with balanced noise and offset performance. The resistors are metal foil resistors with ultra-low temperature coefficient and high accuracy. A fully differential amplifier (FDA) circuit is inserted between the amplification circuit and the analog-to-digital converter (ADC). It realizes single-ended to differential conversion and implements a multi-feedback second-order Bessel filter with 10 kHz bandwidth. The FDA circuit drives a high-precision successive approximation register (SAR) type ADC, which has a high signal-to-noise ratio, high linearity and low distortion, facilitating accurate signal sampling.

## 2.2 Read-out and Control Design

The readout and control module consists of an FPGA-based digital circuit and host computer software. Its structure is illustrated in fig. 4. The digital circuit is designed isolated from the front-end through 100 MHz high-speed digital isolators. This design disrupts the ground loop of the analog and digital circuits, thus reducing the interference and noise affecting the sensitive analog circuit. The analog circuit is independently powered by two batteries and a battery management system (BMS), in order to achieve low-noise power supply, and it is covered by two-layer shieldings.

The FPGA logic is designed to be flexible, and supports two-channel multi-ports data readout. Port A is the output data of a SINC1 digital filter, which exhibits less overshoot and higher waveform accuracy. This data can be utilized for system debugging as it has high data readout rate (23 kSPS) and represents the amplified voltage waveform. The port A data is then differentiated by a differentiating logic to convert integrated waveform into a dc output (port D). This is implemented by subtracting two adjacent data points, and the differentiation process is in real-time. The digital circuit is designed to be flexibly configurable, enabling software access to both the filtered waveform and the differentiated measurements.

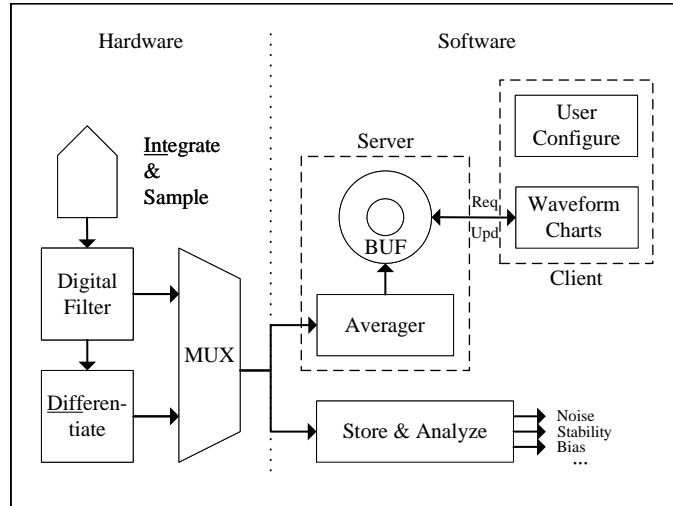


**Figure 4.** Architecture of the SCMS. It involves hardware amplification and digitization of the input current, with subsequent data analysis performed in software.

The data is transmitted using a universal serial bus (USB) interface to the host software. The system’s software is developed in Python, enabling online user configuration, data storage, display, and offline analysis. For online display and configuration, the system employs a web browser/server (B/S) architecture to facilitate remote multi-user access. Within the browser client, users can configure the display settings and hardware parameters for sampling and filtering. The server uses a repeat average filter to combine data points per  $n$  power line cycles (PLC), thus reducing noise glitches and decreasing the data rate. The processed data is stored in a ring buffer, periodically extracted by the user client to update waveform charts. Additionally, the software supports comprehensive offline analysis with detailed analysis methods outlined in Section 3.

### 3 Performance Test Platforms and Results

Our prior research evaluated the system’s performance by testing its noise level, output offsets, and transient response[14]. However, some crucial specifications, such as the stability of the amplification gain and the inherent current bias and noise, which significantly impact precision, could not be tested using the existing setup. Therefore, the platforms and methods for precisely testing these performance are investigated.

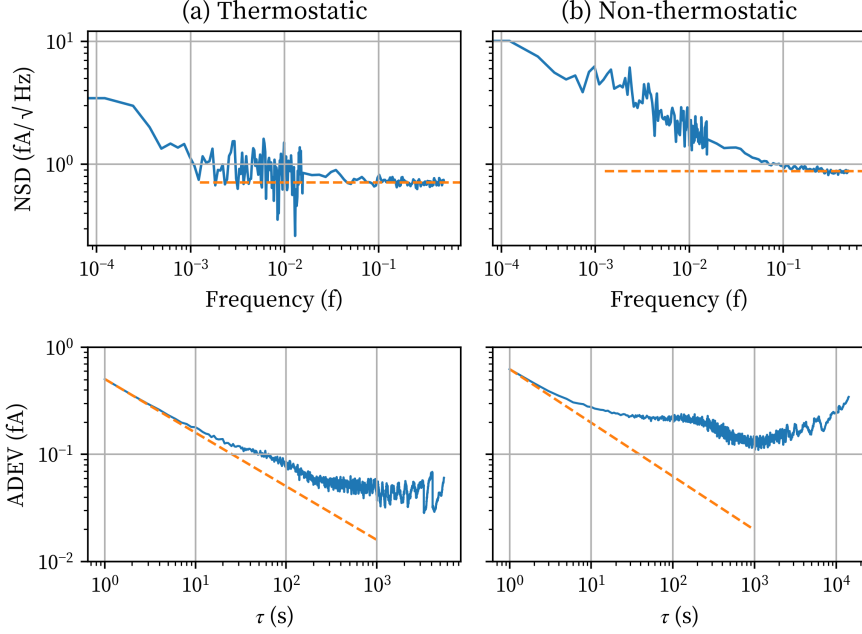
#### 3.1 Current Bias and Noise Tests

The current input cable is a 0.3 m low-noise triaxial cable with double-layer shielding, designed to minimize the triboelectric effect. One side of the cable is connected to the SCMS, while the other side is opened and shielded with a metal cap. We continuously sampled data for several hours, filtered it, and calculated the noise spectral density (NSD) and the Allan deviation (ADEV) offline.

To research the influence of the environment temperature, a built-in temperature sensor is employed to record the temperature of the system. The temperature sensor is placed near the integrating capacitor array. We tested in both thermostatic and non-thermostatic environments.

**Table 2.** Current Bias Measurement Results

| temperature range                     | current bias range  | averaged current bias |
|---------------------------------------|---------------------|-----------------------|
| 26.8 °C to 27.1 °C (thermostatic)     | −0.19 fA to 0.62 fA | 0.24 fA               |
| 26.9 °C to 27.9 °C (non-thermostatic) | −2.91 fA to 0.01 fA | −1.02 fA              |

**Figure 5.** Noise test results analyzed by NSD and ADEV.

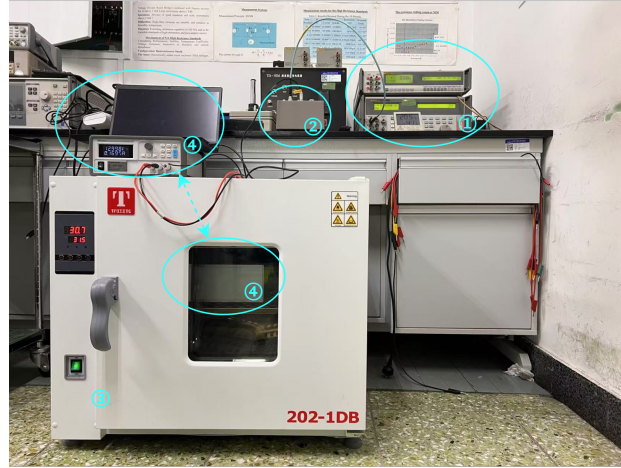
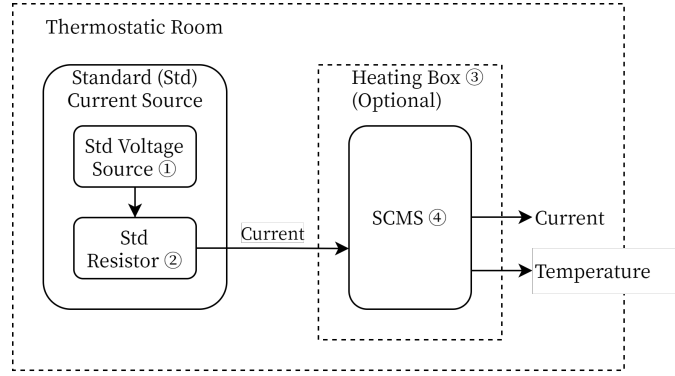
The fluctuations of the current bias and temperature for both tests are listed in table 2. The current measurements are filtered by a moving averager with a window of 100 s to reduce noise interference.

Figure 5 depicts the noise performance of the system, and the current measurement data is the same as the bias current test. Results indicate that in both thermostatic and non-thermostatic environments, the system has a low white noise level of  $0.7 \text{ fA}\sqrt{\text{Hz}}$  and  $0.9 \text{ fA}\sqrt{\text{Hz}}$ . In DC measurements, consecutive data sampling and averaging are commonly used for improving precision. ADEV is widely used for characterizing the noise and fluctuations in low-level measurement instruments [18, 19]. The slow fluctuations of the temperature induced low-frequency current fluctuations, and elevated the ADEV in non-thermostatic condition. The lowest ADEV, which is also called "bias stability", is about  $0.04 \text{ fA}$  in thermostatic environment. ADEV can be used to evaluate the impact of both white noise and low-frequency noise on data variability under different integrating time  $\tau$ . The orange straight lines represent the white noise contributions. In ADEV plots, they are calculated by

$$\sigma_w = \sqrt{S_w/2\tau}, \quad (3.1)$$

where  $S_w$  is the white NSD[20]. Compared with our previous design that employed CMOS-based reset switch (with an current bias of  $100 \text{ fA}$  level and a noise level of  $7 \text{ fA}\sqrt{\text{Hz}}$ )[14], the noise and bias performance have been significantly improved.





**Figure 6.** Stability tests setup. The heating box is optional, and dedicated to be used in temperature dependency test.

### 3.2 Stability Tests

The stability performances of the SCMS gain includes short-term stability, temperature dependency, linearity and long-term reproducibility. A test platform is built utilizing the standard small current source equipment at NIM China, as shown in fig. 6. The standard current source comprises a standard voltage source (Fluke 5520A) and a standard resistor (Keithley 5156). The standard equipment is calibrated regularly at NIM China, and the key parameters are presented in tables 3 and 4. The current NSD of Keithley 5156 is estimated using resistor thermal noise equation

$$I_N = \sqrt{4kT/R}, \quad (3.2)$$

where  $k$  is the Boltzmann constant,  $T$  is the Kelvin temperature and  $R$  is the resistance. This standard equipment is the most precise calibrator currently available.

The testing uncertainties of the short-term tests (including temperature dependency and linearity tests) rely on the short-term stability of the standard equipment. Since our primary focus is on the relative fluctuations of the gain, the standard equipment calibration error, as a systematic error, will not affect the test results. It comprises the stability of the voltage source (shown in table 3) and the resistor. The resistor's stability mainly stems from the temperature coefficient. As we observed,

**Table 3.** Fluke 5520A Standard Voltage Source Parameters

| parameters                | 330 mV range              | 3.3 V range                      | 33 V range                      | note                                 |
|---------------------------|---------------------------|----------------------------------|---------------------------------|--------------------------------------|
| peak-peak noise           | 1 $\mu$ V                 | 10 $\mu$ V                       | 100 $\mu$ V                     | 0.1 Hz to 10 Hz                      |
| equivalent voltage NSD    | 53 nV/ $\sqrt{\text{Hz}}$ | 0.53 $\mu$ V/ $\sqrt{\text{Hz}}$ | 5.3 $\mu$ V/ $\sqrt{\text{Hz}}$ | estimated as white noise             |
| short-term stability      | 3ppm+1 $\mu$ V            | 2ppm+1.5 $\mu$ V                 | 2ppm+15 $\mu$ V                 | 24 hours, $\pm 1$ $^{\circ}\text{C}$ |
| long-term reproducibility | 15ppm+1 $\mu$ V           | 9ppm+2 $\mu$ V                   | 10ppm+20 $\mu$ V                | 90 days, $\pm 5$ $^{\circ}\text{C}$  |

**Table 4.** Keithley 5156 Standard Resistor Parameters

| parameters              | 1 G $\Omega$                | 10 G $\Omega$               | 100 G $\Omega$               |
|-------------------------|-----------------------------|-----------------------------|------------------------------|
| current NSD             | 4.07 fA/ $\sqrt{\text{Hz}}$ | 1.29 fA/ $\sqrt{\text{Hz}}$ | 0.41 fA/ $\sqrt{\text{Hz}}$  |
| temperature coefficient | <25 ppm/ $^{\circ}\text{C}$ | <25 ppm/ $^{\circ}\text{C}$ | <100 ppm/ $^{\circ}\text{C}$ |
| voltage coefficient     | <1 ppm/V                    | <1 ppm/V                    | <1 ppm/V                     |

in a single test, the temperature fluctuation is less than 0.5  $^{\circ}\text{C}$ . Therefore, the short-term stability of the resistor is considered to be 13 ppm of 1 G $\Omega$  and 10 G $\Omega$ , and 50 ppm of 100 G $\Omega$ . The total relative error of this standard equipment is calculated under the worst-case scenario (where the correlation coefficient between the voltage and resistor is -1), and the formula is

$$\delta_{\max} = |\delta_u| + |\delta_r|, \quad (3.3)$$

where  $\delta_u$  and  $\delta_r$  are the relative stability errors of the voltage source and the resistor. This is regarded as the limiting error, so the coverage factor  $k$  is taken as 3.

To suppress low-frequency noise and drift effects[18], the currents are periodically reversed (every 600 s), and the first 50 s samples after current reversal are discarded to allow the current to stabilize. We define the normalized gain ( $G_{\text{nom}}$ ) as the measured current value  $I_m$  divided by the standard source current  $I_s$ , as shown below:

$$G_{\text{nom}} := \frac{I_m}{I_s}. \quad (3.4)$$

$I_m$  and current bias  $I_b$  can be computed from the positive and negative current measurements ( $I_{m+}$  and  $I_{m-}$ ) as follows:

$$I_m = \frac{1}{2} (I_{m+} - I_{m-}), \quad (3.5)$$

$$I_b = \frac{1}{2} (I_{m+} + I_{m-}) / G_{\text{nom}}. \quad (3.6)$$

Each measurement corresponds to the averaged result obtained over a current reversion period of 1200 s.

During the short-term stability test, the standard equipment used the 10 G $\Omega$  resistor and the 1 V voltage output to generate a 100 pA current. Figure 7 shows the fluctuations of both the normalized gain  $G_{\text{nom}}$  and current bias  $I_b$  during the short-term stability test. The bias current is the sum of that of the SCMS and the standard equipment. Based on table 2, it is believed that the standard equipment plays a dominant role in the bias current result.

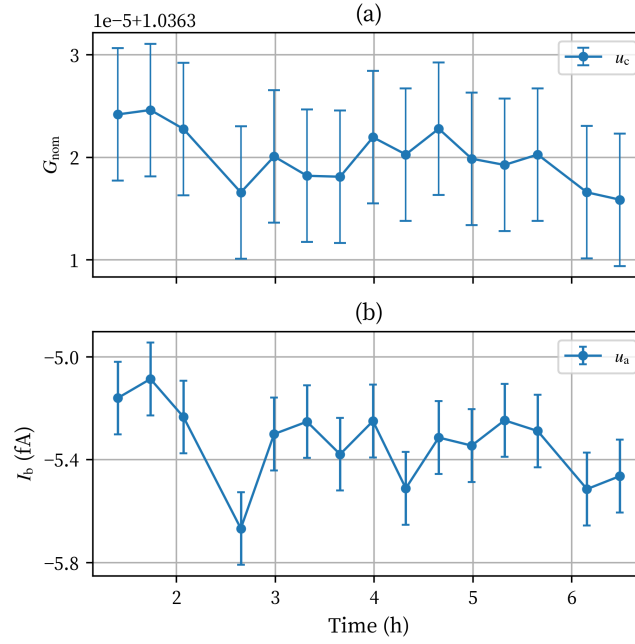


**Figure 7.** Short term stability test result. Here,  $u_c$  represents the standard combined uncertainty, while  $u_a$  stands for the Type A uncertainties.

The ADEV is utilized to evaluate the data variability of the  $G_{\text{nom}}$ , the calculation formula is as follows:

$$\sigma_y = \sqrt{\frac{\sum_{k=1}^{N-1} [I_m(k+1) - I_m(k)]^2}{2 \cdot (N-1)}}, \quad (3.7)$$

where  $N$  is the number of the measurements. The ADEV can be considered as a Type A standard uncertainty ( $u_a$ ), which amounts to 1.9 ppm. The Type B standard uncertainty ( $u_b$ ) is calculated based on the short-term stability of the standard equipment in eq. (3.3) and is 6.2 ppm. In total, the standard combined uncertainty ( $u_c$ ) of the normalized gain is 6.5 ppm. All uncertainties are presented in the form of relative values. We found that there is a 3.63% deviation between the normalized gain and its nominal value of 1. This is attributed to the parallel parasitic capacitance as previously analyzed.

The temperature coefficient of the standard current source equipment at NIM China is inadequate for accurately evaluating the temperature dependency of the SCMS. Therefore, we came up with an idea of placing the standard device in the thermostatic room to guarantee the stability of the test current, while placing the SCMS inside a heating box to vary its temperature. Before this test, the instruments had been preheated for one hour. Moreover, after each temperature alteration, we waited for one hour to allow the temperature to stabilize.

The test result is shown in fig. 8. There is an obvious correlation between the gain and the temperature, and the coefficient of determination ( $R^2$ ) for the linear fit is 0.91. According to the linear regression analysis, the slope represents the temperature coefficient of the SCMS, which is about  $2.1 \pm 1$  ppm/ $^{\circ}\text{C}$ . The integrated temperature sensor of the SCMS has a very low reproducibility error of 32 m $^{\circ}\text{C}$ , so that it's negligible.

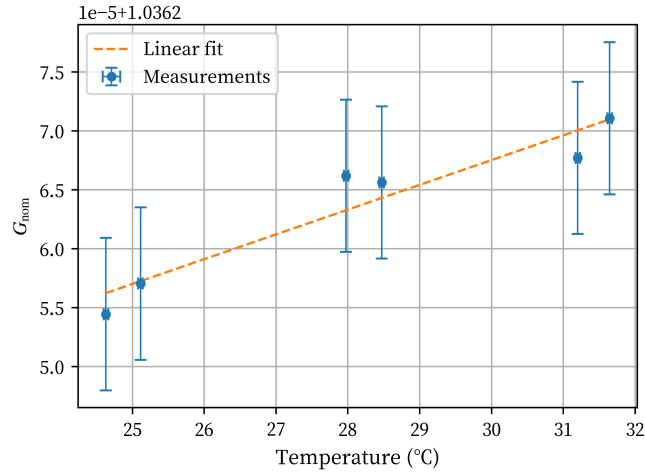


**Figure 8.** Temperature dependency test result.

**Table 5.** Current Values and Uncertainties in the Linearity Test

| input current | voltage | $u_c$   |
|---------------|---------|---------|
| 100 pA        | 10 V    | 19 ppm  |
| 30 pA         | 3.0 V   | 20 ppm  |
| 10 pA         | 1.0 V   | 27 ppm  |
| 3.0 pA        | 300 mV  | 68 ppm  |
| 1.0 pA        | 100 mV  | 200 ppm |
| 300 fA        | 30 mV   | 650 ppm |
| 100 fA        | 10 mV   | 0.19 %  |
| 30 fA         | 3.0 mV  | 0.65 %  |
| 10 fA         | 1.0 mV  | 1.9 %   |

For the linearity test, the standard resistor is set to  $100\text{ G}\Omega$ , and we adjust the standard voltage output to obtain a small current ranging from 10 fA to 100 pA. We use the fixed resistor to mitigate the impact of calibration errors of different resistors.  $u_a$  in this test is the same as that in the short-term stability test, and  $u_b$  of different current values are estimated using the same method. In fact,  $u_a$  can be lower since we use a larger resistor that generates less thermal noise. The standard uncertainties corresponding to each current measurement are listed in table 5.

The linear test result is shown in fig. 9. The measured current and the input current are highly correlated, with a coefficient of determination ( $R^2$ ) greater than 0.999,999,999. The residual errors are plotted in subfigure (b). The maximum residual error is 1.4 fA and the standard deviation of the residuals is 0.86 fA.

Utilizing the same test platform, we assessed the linearity and short-term stability of a commercial digital picoammeter, the Keithley 6430. The 100 pA range along with the highest-accuracy mode of this instrument was selected for comparison with the SCMS, and the moving average and median average filters were disabled. The results of short-term stability and linearity tests are

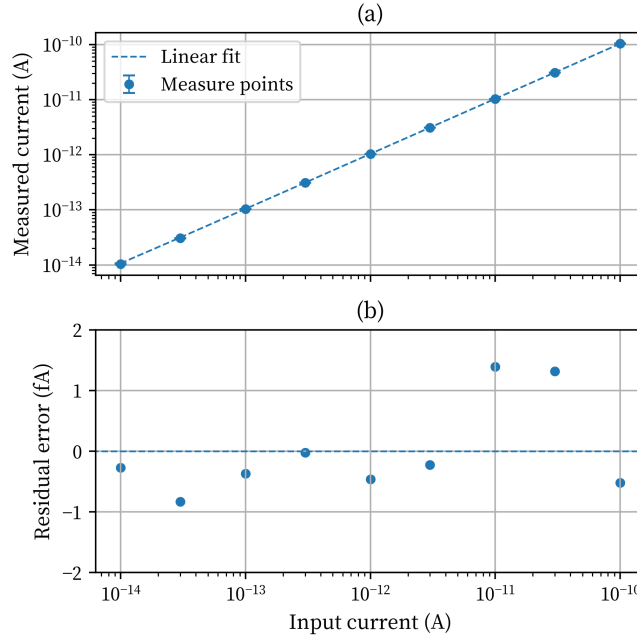


**Figure 9.** Linearity test result.

presented in fig. 10, The ADEV with a 1200 s integration time in the short-term test is 1.6 ppm, and the standard deviation of the residuals is 0.58 fA. In these two tests, Keithley 6430 and the SCMS exhibit similar performances. However, as its temperature coefficient, which we calculated from the datasheet, is at the 100 ppm/ $^{\circ}$ C level, it is much larger than that of the SCMS.

The input voltage burden  $V_b$  of the SCMS was also tested. We used a nanovoltmeter (Keithley 2182) to measure the voltage difference between the current input (through a buffer) and the ground. For both the input current of  $\pm 100$  pA and  $\pm 10$  pA, the  $V_b$  remained stable at around 33  $\mu$ V. For comparison, the  $V_B$  of Keithley 6430 is larger and exhibits instability in response to variations in the input current [18].

### 3.3 Long-term Reproducibility Test Utilizing Ionization Chamber

Since the standard current source equipment at NIM China cannot be occupied for a long time, the long-term stability of the SCMS was tested using an IC and a radioactive source with a long half-life. The IC is a  $4\pi\gamma$  ionization chamber manufactured in China, and it's connected to the SCMS through a 0.3 m-long low-noise triaxial current cable. A voltage of 600 V is applied to provide the polarization electric field to the IC. The test setup is illustrated in fig. 11.

The noise performance when using an IC is more complex than that of the SCMS itself. This is because the equivalent capacitance model of the IC increases the noise gain of the amplification circuit, and the high-voltage source introduces excess noise[21, 22]. In this research, several ICs and high-voltage sources were combined to conduct a preliminary assessment of the NSD, following which the combination with the lowest noise was selected. A  $^{226}\text{Ra}$  radioactive source was employed, which has a long half-life of approximately 1600 years. Thus, during the one-month testing period, the attenuation is only 36 ppm and can be considered negligible. During the test, the

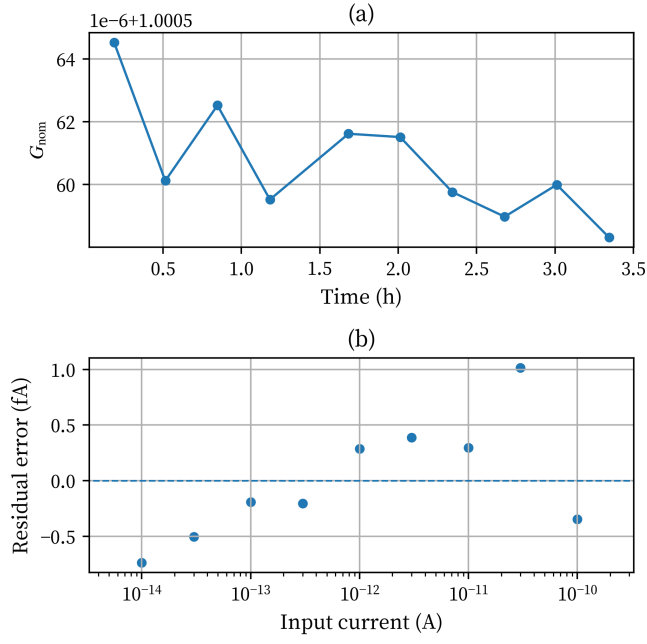


**Figure 10.** Stability test results of Keithley 6430 for comparison.

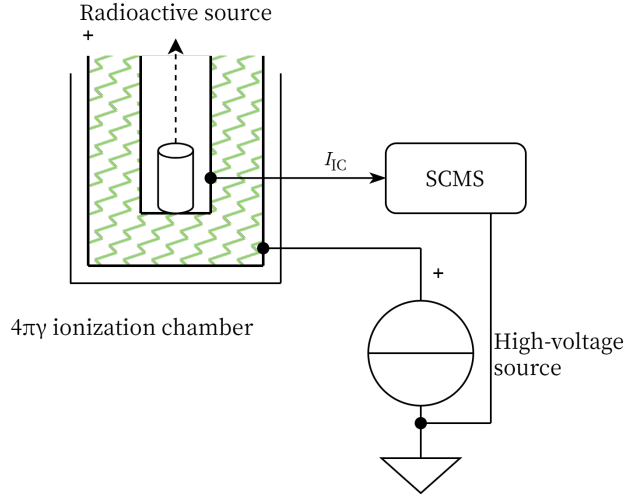


**Figure 11.** Ionization chamber test platform.

test platform was placed in an air-conditioned room. On average, the tests were carried out twice a week. For each measurement, a preheating process lasting 1.5 h was performed first, followed by a 30 min measurement of the IC's background current ( $I_{bg}$ ), and then a 30 min measurement of the ionization current  $I_{ic}$ . The background-free measurement result is calculate as follows:

$$I_m = \bar{I}_{ic} - \bar{I}_{bg}. \quad (3.8)$$

The duration of a single measurement is kept within 1 h to reduce the error caused by the background

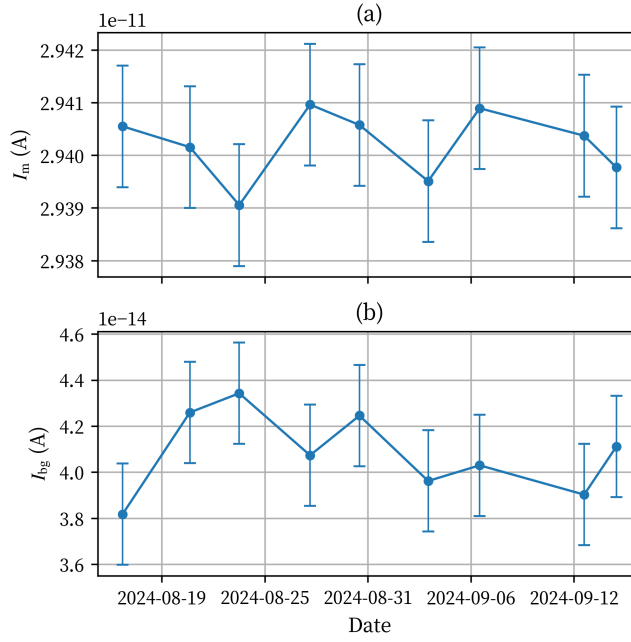


**Figure 12.** Long-term reproducibility test results. The error bars represent the  $u_a$ .

current fluctuation[23].

The results of the long-term reproducibility test are shown in fig. 12. To evaluate the  $u_a$  of this test, we continuously repeated the measurements ( $I_m$ ) several times after preheating. And then we used the difference between two adjacent measurements to calculate the ADEV by applying eq. (3.7). The ADEV for  $I_m$  and  $I_{bg}$  tests are 12 fA and 2.2 fA, respectively, and the averaged values of  $I_m$  and  $I_{bg}$  during this test are 29.4 pA and 40.8 fA. Due to the complexity of the  $u_b$  in the IC test, we do not discuss it in this study.

## 4 Conclusions

A high-precision measurement system for pA level small direct currents has been developed. It is intended to replace the commercial picoammeter and be applied to the  $4\pi\gamma$  IC radioactivity standard at NIM, China, thereby improving the ionization current measurement capability. Meanwhile, it can serve as a high-precision digital picoammeter, which has broad application prospects in the fields of physical experiments and fundamental metrology. The SCMS has been optimized on its gain stability and noise performance. Through simulations, the configuration of the capacitor array was optimized to mitigate the impact of parasitic capacitance on gain. Meanwhile, the primary source of noise and current bias has been identified and reduced by using a relay as the reset switch. Furthermore, the digital readout and control module has been upgraded to enhance its flexibility and functionalities.

The test setups for noise and stability were conducted using the standard small current source equipment and the IC. The SCMS exhibits a low noise floor of less than  $1 \text{ fA}\sqrt{\text{Hz}}$ , and low current bias of less than 1 fA typically. The noise and bias performance is further improved compared

to the previous work. In terms of stability, the gain of the SCMS has a very low temperature coefficient (2 ppm/°C), as well as short-term stability and linearity indicators similar to those of Keithley 6430. The long-term reproducibility was also studied by using an  $4\pi\gamma$  IC, and reasonable test results were obtained. In future work, we plan to conduct in-depth research on the electronic model and complex error sources of the IC, so as to further improve the measurement capability of the ionization current.

## Acknowledgments

This work was supported by the NIM, China. We would like to express our gratitude to Bo Liang from the Electromagnetic Metrology Division of NIM China, for providing the test conditions and her valuable suggestions for this work.

## References

- [1] PTB, *Improved current measurement on ionization chambers – a milestone for activity and half-life determinations*, Jan., 2021.
- [2] D. Drung, M. Götz, E. Pesel and H. Scherer, *Improving the Traceable Measurement and Generation of Small Direct Currents*, *IEEE Transactions on Instrumentation and Measurement* **64** (2015) 3021.
- [3] S.D. Torre, B. Gobbo, S. Levorato, G. Menon and F. Tessarotto, *RHIP, a radio-controlled high-voltage insulated picoammeter*, in *2016 IEEE Nuclear Science Symposium, Medical Imaging Conference and Room-Temperature Semiconductor Detector Workshop (NSS/MIC/RTSD)*, pp. 1–3, Oct., 2016, DOI.
- [4] M. Crescentini, M. Bennati, M. Carminati and M. Tartagni, *Noise Limits of CMOS Current Interfaces for Biosensors: A Review*, *IEEE Transactions on Biomedical Circuits and Systems* **8** (2014) 278.
- [5] D. Drung, C. Krause, U. Becker, H. Scherer and F.J. Ahlers, *Ultrastable low-noise current amplifier: A novel device for measuring small electric currents with high accuracy*, *Review of Scientific Instruments* **86** (2015) 024703.
- [6] G. Sobolewski and L.M. Klubert, *Source measure unit current preamplifier*, May, 2000.
- [7] “B2980B Series Femto/Picoammeter and Electrometer/High Resistance Meter.”
- [8] J. Wang, B.K. Li, L.B. Ruan, G. Tian, X.B. Li and H.G. Qu, *A High Precision Pico-Amperes Scale Current Measurement System in Radiation Detection*, *Applied Mechanics and Materials* **239-240** (2013) 145.
- [9] A.A. Mortuza, M.F. Pervez, M.K. Hossain, S.K. Sen, M.N.H. Mia, M.K. Basher et al., *Pico-current Measurement Challenges and Remedies: A Review*, *Universal Journal of Engineering Science(CEASE PUBLICATION)* **5** (2017) 57.
- [10] A. Utrobicic, M. Kovacic, F. Erhardt, N. Poljak and M. Planinic, *A floating multi-channel picoammeter for micropattern gaseous detector current monitoring*, *Nuclear Instruments and Methods in Physics Research Section A: Accelerators, Spectrometers, Detectors and Associated Equipment* **801** (2015) 21.
- [11] S. Epure, R. Belea and L. Frangu, *Low-cost picoammeter for dielectrics*, in *2013 IEEE 19th International Symposium for Design and Technology in Electronic Packaging (SIITME)*, pp. 95–98, Oct., 2013, DOI.
- [12] *The Axon Guide for Electrophysiology and Biophysics Laboratory Techniques*, Sept., 2021.



- [13] M. Crescentini, M. Tartagni, H. Morgan and P.A. Traverso, *A compact low-noise broadband digital picoammeter architecture*, *Measurement* **100** (2017) 194.
- [14] S. Liang, K. Song, C. Zhu and J. Liang, *A Low-Noise Int-Diff Small Direct Currents Measurement System With Two-Stage Amplifier and Digital Differentiator*, *IEEE Transactions on Nuclear Science* **70** (2023) 954.
- [15] M. Bennati, F. Thei, M. Rossi, M. Crescentini, G. D'Avino, A. Baschiroto et al., *A Sub-pA Delta-Sigma Current Amplifier for Single-Molecule Nanosensors*, in *2009 IEEE International Solid-State Circuits Conference - Digest of Technical Papers*, pp. 348–349,349a, Feb., 2009, DOI.
- [16] R.A. Baumgartner, *Systems and methods for measuring picoampere current levels*, Feb., 2006.
- [17] F. Salvaire, *Circuit simulation using Python*, July, 2017.
- [18] H. Scherer, D. Drung, C. Krause, M. Götz and U. Becker, *Electrometer Calibration With Sub-Part-Per-Million Uncertainty*, *IEEE Transactions on Instrumentation and Measurement* **68** (2019) 1887.
- [19] T. Witt, *Using the Allan variance and power spectral density to characterize DC nanovoltmeters*, *IEEE Transactions on Instrumentation and Measurement* **50** (2001) 445.
- [20] J. Rutman and F. Walls, *Characterization of frequency stability in precision frequency sources*, *Proceedings of the IEEE* **79** (1991) 952.
- [21] S.P. Giblin and G. Lorusso, *Exploring a new ammeter traceability route for ionisation chamber measurements*, *Review of Scientific Instruments* **90** (2019) 014705.
- [22] C. Cottini, E. Gatti, G. Giannelli and G. Rozzi, *Minimum noise pre-amplifier for fast ionization chambers*, *Il Nuovo Cimento (1955-1965)* **3** (1956) 473.
- [23] R. Fitzgerald, D.E. Bergeron, S.P. Giblin, D.G. Jarrett, S.M. Judge, C. Michotte et al., *The next generation of current measurement for ionization chambers*, *Applied Radiation and Isotopes* **163** (2020) 109216.